

Electronic Light Scattering Drives Optical Heating of Nonlocal Media

S.S. KHARINTSEV^{1*} AND E.I. BATTALOVA¹

¹*Department of Optics and Nanophotonics, Institute of Physics, Kazan Federal University, Kremlevskaya str., 16a, Kazan, 420008, Russia*

[*skharint@gmail.com](mailto:skharint@gmail.com)

Abstract: Light absorption in opaque solids is directly governed by optical transitions between the electronic states near the bandgap. This physical mechanism underlies the optical heating of a medium that efficiently absorbs light at resonance. However, such a strategy is true for a homogeneous bulk medium that is temporally dispersive. This work focuses on the optical heating of spatially dispersive (or nonlocal) materials due to broadband inelastic light scattering rather than absorption. A light-induced optical inhomogeneity (vacancy, ad-atom, etc.) produces an optical near-field photon with expanded momentum that enhances light-matter interaction. As a result, indirect optical transitions become accessible throughout the entire Brillouin zone due to electron-photon momentum matching. The real refractive index of nonlocal media can greatly increase over a wide spectral range beyond resonance. According to the Kramers-Kronig relation, such nonlocal media can capture light solely through electronic light scattering. Herein, we experimentally demonstrate this effect by melting spatially confined semiconductors (silicon atomic-force-microscopy cantilever) and metals (gold shear-force-microscopy tip) under off-resonance continuous-wave laser pump. Light scattering based on electron-photon interaction becomes the dominant physical process in media with strong spatial dispersion. These findings will be critical for cutting-edge technologies in optoelectronics, photovoltaics, and biomedicine.

Keywords: electronic light scattering, electron-photon interaction, near-field photon momentum, optical heating, spatial dispersion, nonlocal medium.

Everyday intuition suggests that optical heating of materials is directly associated with light absorption. This physical process plays a paramount role in most areas of photonics and optical spectroscopy.¹⁻⁵ Though this phenomenon is generally well understood in homogeneous bulk matter, it seemingly requires rethinking of light-matter interaction in heterogeneous (nonlocal) media.⁶ The real refractive index n and the extinction coefficient κ are fundamental

optical constants driving scattering and absorption of light, respectively (Fig. 1a).⁷⁻⁹ Both processes can perturb an equilibrium of the electron system, leading to spatial-temporal fluctuations of charge density $\rho(\mathbf{r}, t) = \rho_0 + \frac{1}{e} \nabla \cdot \mathbf{P}(\mathbf{r}, t)$ (ρ_0 is the equilibrium charge density, e is the electron charge, $\mathbf{P}(\mathbf{r}, t)$ is the electric polarization of medium).¹⁰ Following M.V. Klein,¹¹ the cycle-averaged charge density $\langle \rho(\mathbf{r}, t) \rangle$ corresponds to a true phase-delay refractive index of homogeneous media in the lack of perturbation, i.e. $n \sim \rho_0$. Since light absorption is a process that is nonlocal in time (Fig. 1a), the change in $\langle \rho(\mathbf{r}, t) \rangle$ and n

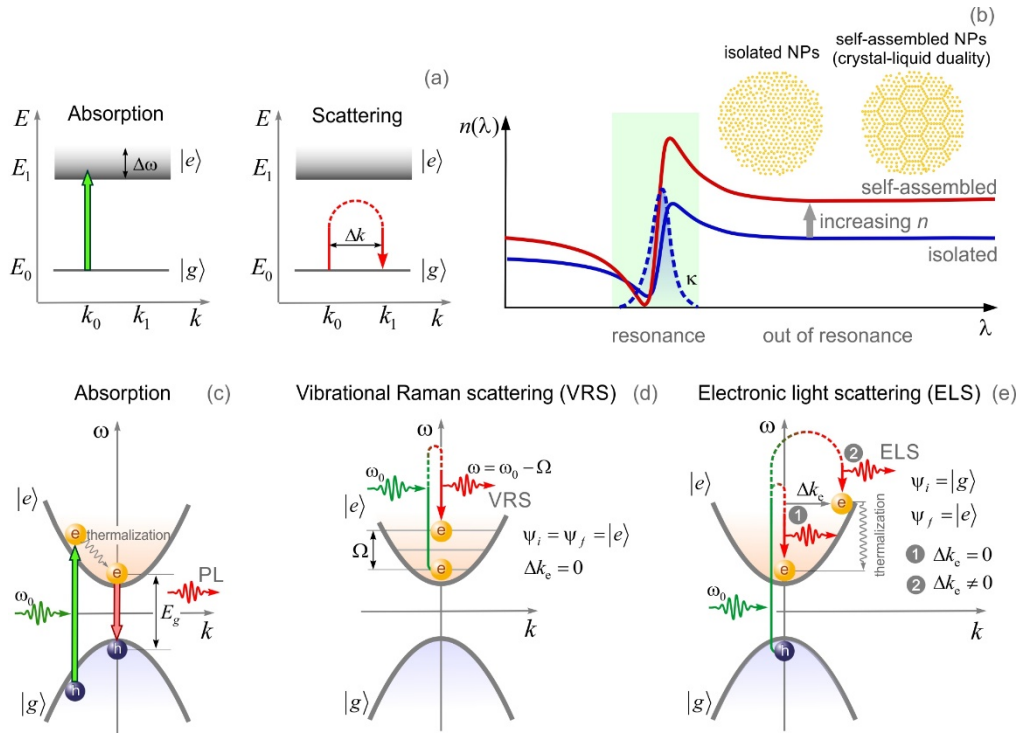


Figure 1. (a) Sketch of two light-matter interaction mechanisms: absorption and scattering. (b) Schematic illustration of the refractive index for isolated and self-assembled NPs. The inset shows isolated and self-assembled (crystal-liquid duality) nanoparticles. Light-matter interaction mechanisms in semiconductors: (c) absorption, (d) inelastic phonon-photon scattering (Raman effect) and (e) electronic light scattering (ELS) without (1) and with (2) a change in the electron momentum.

is associated with temporal dispersion at resonance (Fig. 1b). The causality principle not only relates n and κ to each other via the Kramers-Kronig formula but also imposes the limitations on them.¹² It has long been believed that the refractive index of naturally occurring materials cannot exceed 4.^{7,9} Recent experimental works have shown that these limitations are no longer valid. Underlying physical mechanisms include gap plasmon resonance excitation in self-assembled gold nanoparticles (Au NPs) ($n = 10.02$),⁴ phase transitions in perovskites ($n = 26$),¹³ infrared plasmon-polariton excitation in a graphene monolayer near a quantum well ($n > 100$).¹⁴ Remarkably, I. Kaminer et al introduced a momentum-dependent confinement factor instead of the phase-delay refractive index that is commonly accepted.^{14,15} The authors highlighted the emerging primacy of spatial non-locality in media involving optical inhomogeneities whose size is comparable to or even less than the wavelength of an incident electromagnetic wave. Herein, the generation of the near-field in close vicinity of an optical inhomogeneity leads to spatially varying refractive index $n(\mathbf{r})$ or spatial dispersion $\nabla[n(\mathbf{r})] = dn/d\mathbf{r}$ (see Section I in the Supplementary Information).^{6,16} However, this effect is insignificant for homogeneous materials and, therefore, is not taken into account in most cases. Strong spatial dispersion occurs, for example, in a crystal-liquid dual system exhibiting long-range order and local disorder that coexist.^{16,17} This class includes self-assembled Au NPs in which the polarization becomes non-uniform throughout the entire volume (the inset in Fig. 1b).¹⁶ Other materials with similar behavior are ceramics and high-entropy crystals,¹⁸ amorphous and porous solids,¹⁹ perovskites,²⁰ liquid crystals,¹⁸ highly-associated liquids,²¹ distilled and micellar water,²² peptides and proteins,²³ to name a few. The interaction of light with spatially dispersive matter forms an emerging field of modern optics, called *nonlocal photonics*. For optically transparent ($\kappa \approx 0$) semiconductors the spatially varying refractive index reads as

$$n^2(\mathbf{r}) = 1 + \frac{e^2}{\pi^2 m_e} \sum_{cv} \int_{BZ} \frac{f_{cv}^{\boldsymbol{\kappa}}(\mathbf{k})}{\Omega_{cv}^2(\mathbf{k}) - \omega^2} d\mathbf{k}, \quad (1)$$

where Ω_{cv} is a vibronic frequency corresponding to optical transitions between the Bloch electronic states $|v\rangle$ and $|c\rangle$, m_e is the effective mass of an electron, $\boldsymbol{\kappa}$ is a light polarization direction. The oscillator strength $f_{cv}^{\boldsymbol{\kappa}}(\mathbf{k})$ is modified as follows

$$f_{cv}^{\boldsymbol{\kappa}}(\mathbf{k}) = \frac{2m_e}{\hbar} |D_{cv}^{\boldsymbol{\kappa}}(\mathbf{k})|^2 \quad (2)$$

here \hbar is the Planck's constant, $D_{cv}^{\boldsymbol{\kappa}}(\mathbf{k}) = \langle c | e^{i\boldsymbol{\kappa} \cdot \mathbf{r}} \partial / \partial \mathbf{r} | v \rangle$ is the transient electrical dipole moment that considers spatial dispersion. In homogeneous media, a change in the refractive index is possible at resonance only (temporal dispersion) through vertical (direct) transitions, leading to absorption (Fig. 1c). Meanwhile, the refractive index is not sensitive to spontaneous vibrational Raman scattering (Fig. 1d) because the electron system remains unperturbed. In Eq.

(1), integration runs over the entire Brillouin zone, and, thus, indirect optical transitions become accessible (Fig. 1e) during which the electron momentum can alter, and it results in photon-momentum-enabled electronic Raman scattering.⁵ This is a specific signature of nonlocal media. As seen from Fig. 1e, thermalization is inevitably followed by optical heating of a light-scattering medium.

This work addresses the optical heating of spatially dispersive semiconductors and metals due to electronic light scattering (ELS). The ELS is based on indirect optical transitions during which the electron momentum can change. This is specifically the mechanism that unravels a number of unusual optical and spectroscopic phenomena that are still poorly understood. These include the optical melting of spatially confined solids under non-resonant cw illumination²⁴ and a nonlinear increase in the intensity of blue-shifted vibrational Raman scattering (VRS) when optical heating.^{25,26}

Optical heating of a temporal-spatial causal medium with a complex permittivity $\varepsilon(\omega, k) = \varepsilon'(\omega, k) + i\varepsilon''(\omega, k)$ (ε' and ε'' are the real and imaginary parts of permittivity) is governed by the absorbed power in volume V :

$$P_{abs} = \int_V \omega \varepsilon_0 \varepsilon''(\omega, k) |\mathbf{E}(\omega, k)|^2 dV. \quad (3)$$

Since $\varepsilon'' = 2n\kappa$,²⁷ there are two contributions to material optical loss: 1) resonant absorption (κ) and 2) inelastic free-electron Drude scattering (n).²⁸ In the former case, light is absorbed by a medium through direct optical transitions between the electronic states near the bandgap. The latter is associated with the attenuation of light due to its inelastic scattering by free charges, Eq. (2) (it reduces to Drude's formula when $\Omega_{cv} = 0$). The attenuation of the intensity of incoming light I_0 when it passes through a homogeneous medium over a distance x exceeding the wavelength λ , is governed by the Beer-Lambert law $I(x) = I_0 \exp[-\alpha x]$, wherein the absorption coefficient $\alpha = 2\omega\kappa/c$ (c is the speed of light in vacuum)²⁷ is solely contributed by κ . Clearly, this formalism is insufficient for understanding an anomalous increase in light absorption (two orders of magnitude) by a Si layer only 2 nm thick, previously discussed in Ref.²⁴ In this work, the authors made conclusions based on the optical melting of a Si AFM cantilever apex (the melting point is 1687 K for bulk Si) and depleted reflection of Si bulk decorated with 1-3 nm diameter Au NPs over all energies above the bandgap of 1.1 eV. However, there are still no solid arguments in favor of absorption driven by indirect transitions under non-resonant pumping. Though this process is also possible,^{29,30} its efficiency is unlikely to be high because of the k -dispersion of energy band.

Fig. 2a schematically shows a TERS setup suitable for measuring the optical heating of spatially confined Si, earlier suggested in Ref.²⁴ In our experiment, a Si AFM cantilever

(VIT_P, NT-MDT) top-illuminated by a focused 633 nm laser light (x100, N.A.=0.7) oscillates in semicontact mode over a borosilicate glass substrate covered with a 50 nm Au film (TED PELLA, Inc.). First, we scan the film surface with the AFM cantilever to visualize its roughness. The size of surface irregularities ranges from 1 to 2 nm (Fig. S3, section III in the SI). Second, the tip apex is positioned over a protrusion with the size of choice: the smaller,

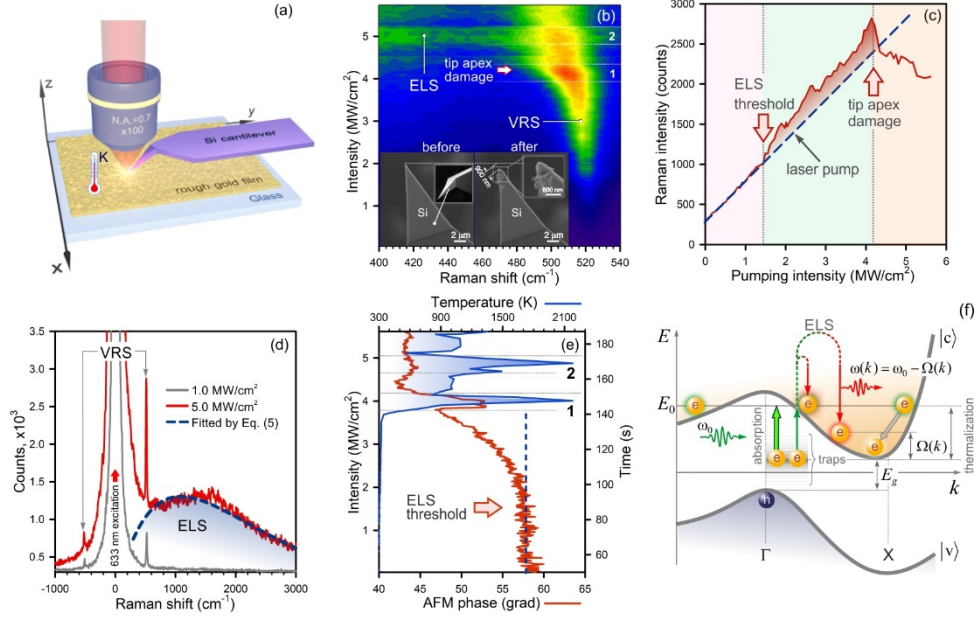


Figure 2. (a) Sketch of a TERS setup (upright configuration). (b) A Raman map of the AFM tip apex exposed to a focused laser light with different pumping intensity (the color indicates Raman intensity). The bottom inset displays SEM images of the AFM cantilever tips before and after laser impact with the intensity of 5 MW/cm². (c) A plot of the VRS intensity vs the pumping intensity. (d) Raman spectra taken at the intensity of 1 MW/cm² (gray) and 5 MW/cm² (red) in Fig. 2 (b). The dashed curve denotes a fit by Eq. (6). (e) A kinetics of the AFM cantilever phase (red) and a dependence of Raman-shift-calculated temperature vs the pumping intensity (blue). (f) The energy-momentum diagram for Si.

the stronger photon confinement is achieved. Upon selecting a 1 nm high protrusion, we then record Raman spectra and the AFM cantilever phase kinetics during gradually increasing the pumping intensity to 5.7 MW/cm² for 140 s. The optical heating is indicated by three observations: i) a temperature-dependent blueshift of the first-order VRS peak of Si at 521 cm⁻¹ (Fig. 2b), ii) high-energy broadband inelastic ELS (Fig. 2d), exhibiting a nonlinear pump-

dependent intensity behavior (Fig. 2c), and iii) a change in the AFM cantilever phase above the pumping intensity of 1.5 MW/cm² (Fig. 2e). The pump-dependent temperature of the tip apex is determined by a Raman-shift-based probe with an accuracy of 50 K (1800 grooves per mm grating) using Eq. S2 (section IV, in the SI). A calibration of the temperature probe was prior performed by temperature-dependent Raman measurements in the range from 25 to 600 °C using a heating stage (Linkam Scientific Model THMS600) (Fig. S4, section 4 in the SI).

Upon turning the level of 4.2 MW/cm² (Fig. 2b and Fig. 2e), the temperature steeply climbs above 2000 K, making the tip apex melted. A close inspection of scanning electron microscopy (SEM) images of the tip apex (the inset in Fig. 2b), visualized before and after laser impact, confirms its destruction within 900 nm extent. However, the AFM cantilever phase starts to respond at 1.5 MW/cm² (red curve, Fig. 2e). The phase shift $\Delta\varphi \approx \frac{Q}{K} \frac{\partial F}{\partial z}$ (where K is the spring constant, Q is the quality factor) is mainly driven by the normal force gradient $\partial F/\partial z$ between the tip apex and the sample, that is greatly sensitive to temperature.^{31,32} It is important to note that the temperature of the entire cantilever remains constant during our experiment, except the tip apex. It follows from the fact that the resonant frequency of the AFM cantilever, equal to 300 kHz, is fixed until the tip apex is damaged, the event marked with the arrow in Fig. 2b. In this figure we highlight two regions labelled as ‘1’ and ‘2’ where giant temperature bursts are seen (Fig. 2e), accompanied by background emission (Fig. 2d). This observation is in good agreement with an increase in the Raman intensity at this level (Fig. 2c) that occurs due to ELS, as follows from Fig. 2d. Large temperature fluctuations above 4 MW/cm² (blue curve, Fig. 2e) are directly related to melting and a change in tip apex morphology. We conclude that the ELS mechanism holds promise for probing a local temperature at the hot spot.

There are two fundamental mechanisms affecting the distribution of charge density or refractive index: 1) absorption and 2) scattering (Fig. 1a). In silicon, that is an indirect bandgap semiconductor, the optical absorption is driven by three-body photon-phonon-electron interaction. On the other hand, this process can be activated using a near-field photon carrying not only energy, but also momentum sufficient for indirect transitions.²⁴ Since the electronic density of states is maximal near the band edge,²⁹ absorption-based indirect transitions are limited because of the k -dispersion of energy band diagram, shown in Fig. 2f. In general, one should consider optical transitions to those electronic states that correspond to energy E_0 . Despite the fact that the transitions supported with large photon momenta are accessible, their contributions to absorption are little. In contrast, light scattering allows indirect transitions to all accessible states below energy E_0 near the conduction band edge. This leads to a broadband inelastic scattering with frequency shifts: $\omega(k) = \omega_0 - \Omega(k)$ (ω_0 is the pumping frequency,

$\Omega(k)$ is a vibronic frequency associated with the energy band), straightforward observed in Fig. 2b and Fig. 2d. It is important to notice that the mechanism of inhomogeneous broadening of a central peak at $\omega(k) \approx \omega_0$ is related to low-energy ELS by Au NPs that exists even at modest pump (Fig. 2d).^{33,34}

The k -dependent ELS intensity is determined by the photonic density of states $\rho(k)$ and the population of electrons, driven by Fermi-Dirac statistics $f_{FD}(k)$, namely:

$$I_{EPS}(k) = C \int \rho(k - k') E(k') f_{FD}(k') dk', \quad (4)$$

where C is a constant proportional the scattering cross-section, $E(k) = \hbar(\omega_0 - \Omega(k))$ is the scattered photon energy. In the simplest case when $\rho(k - k') = I_0 \delta(k - k')$ (I_0 is the incident intensity, $\delta(k - k')$ is the Dirac-delta function), one gets

$$I_{EPS}(k) = C \frac{E(k)}{e^{\frac{E(k)-E_p}{k_B T}} + 1} I_0 \cong CE(k) e^{-\frac{E(k)-E_p}{k_B T}} I_0, \quad (5)$$

where k_B is the Boltzmann constant, T is a temperature. This formula serves as a good approximation provided that high spatial homogeneity ($\rho(k) \sim \delta(k)$) and $E(k) - E_p \gg k_B T$. In Eq. (5), we introduced an additional parameter E_p analogous to Penn energy.³⁵ This seminal concept specifies the energy at which the electronic density of states is maximum throughout the entire Brillouin zone.⁹ In our model, this parameter $E_p = \hbar\omega_0 - \hbar\Omega(k_p)$ denotes the frequency shift corresponding to the statistical mode of near-field photon momentum k_p . This shift tends to zero for electrons trapped near the conduction band edge and basically contributes to low-energy ELS peak. This is the reason why the central peak is dominant in spatially confined metals wherein indirect transitions in the vicinity of the Fermi level occur. Eq. 5 can be used for fitting the high-energy ELS peak at 5 MW/cm² (Fig. 2d), by using the regularized least squares method that yields the Penn energy $E_p = 136$ meV (1100 cm⁻¹).

A hallmark of ELS is the optical heating due to electron thermalization in media with the k -dispersion (Fig. 2f). It is contributed by the slope of the energy band dE/dk and the population of electrons governed by Fermi-Dirac statistics. This means that the change in overall temperature without heat transfer to the environment can be estimated using the following formula:

$$\delta T = \frac{1}{k_B} \int_{BZ} \frac{dE(k')}{dk'} f_{FD}(k') dk'. \quad (6)$$

Eq. (6) indicates the fact that solids with the flat energy band valley is not heated under sub-band pump, and vice versa. The net temperature rise of the tip apex is mainly determined by thermal conductivity of the tip shaft served as a heatsink, whereas heat exchange with the surroundings through its surface (Kapitza resistance³⁶) is negligible.

Anomalous optical heating of spatially dispersive silicon is provided by near-field photons generated by a rough Au film (Fig. 2a). Clearly, the film itself should get heated as well. Due to the high thermal conductivity of the Au film, equal to 320 W/mK, the film is rapidly thermalized and, therefore, it is not heated.

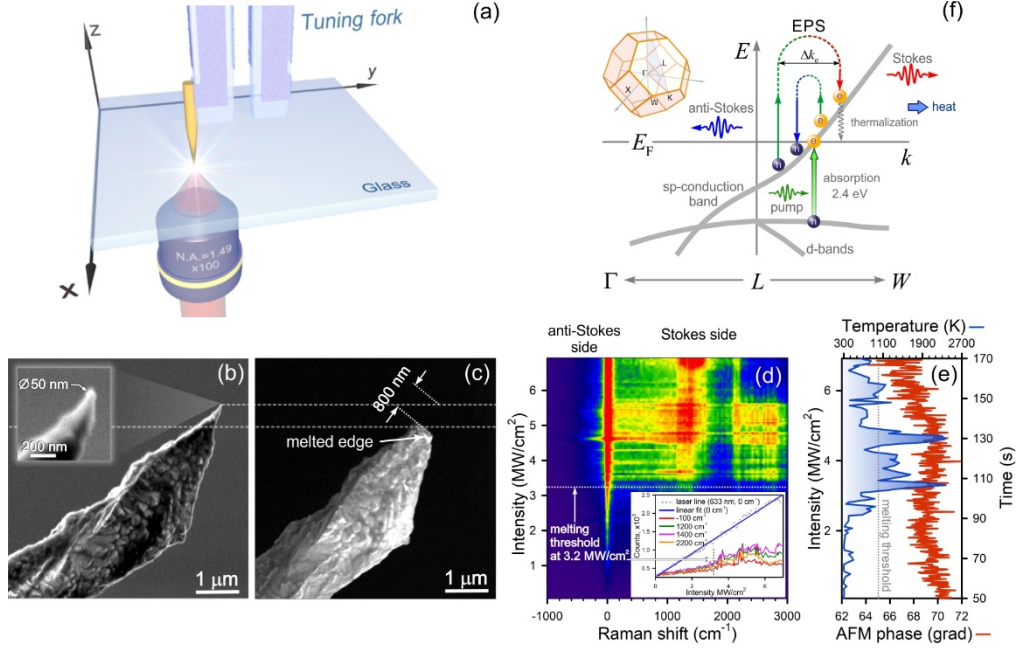


Figure 3. (a) Sketch of a TERS setup (inverted configuration). SEM images of a rough Au tips before (b) and after (c) laser illumination with the intensity of 5 MW/cm². (d) A Raman map of the Au tip upon optical heating. The inset shows a dependence of Raman intensity vs pumping intensity for different wavenumbers. (e) A kinetics of the Au tip phase (red) and a dependence of temperature (blue) vs pumping intensity when illuminated by a 633 nm laser light. (f) Schematic illustration of anti-Stokes/Stokes ELS with varying electron momentum Δk_e and interband absorption in gold. The up-left inset shows the Brillouin zone for gold bulk.

Let us now consider the spatial confinement effect for Au. Fig. 3a shows a bottom-illumination TERS setup in which a rough gold tip glued to a quartz tuning fork oscillates in a plane parallel to the surface of bare coverslip with a frequency of 32 kHz. The inset in Fig. 3b displays a rough gold tip of 25 nm in curvature radius. Using the same protocol as for Si, we detect optical melting of the Au tip apex within 800 nm extent. This paradoxical result is explained by the fact that the melting points of Si (1687 K) and Au (1337 K) differ by 30%, whereas their thermal conductivities (150 W/mK and 320 W/mK, respectively) are two-fold distinct. In this case, a near-field photon is directly generated at the Au tip apex that is first

heated and then destroyed. We detect not only a low-energy ELS signal that is wide-spread for spatially confined metals, but also a broadband high-energy ELS band (Fig. 3d). The optical melting occurs upon the intensity of 3.2 MW/cm². As with Si, the ELS intensity increases above this threshold (the inset in Fig. 3d). Since the Q-factor of the tuning fork is significantly worse than that of the AFM cantilever, the shear-force-microscopy phase is less sensitive to temperature (red curve in Fig. 3e). Following Sheldon et al, we used a combination of both Bose-Einstein and Fermi-Dirac statistics as a fitting function for estimating a temperature inside the Au tip apex by using the regularized least squares method:³⁷

$$f_{\chi}(E, T) = \chi f_{FD}(E, T) + (1 - \chi) f_{BE}(E, T), \quad (7)$$

where χ is a relative contribution of both to the distribution. The melting temperature correlates well with the threshold value at which the ELS intensity starts to increase in Fig. 3d. Multiple temperature spikes are caused by dynamical destruction of the tip apex upon cw illumination (blue curve, Fig. 3e). Unlike semiconductors, indirect optical transitions in spatially dispersive metals occur near the Fermi level, contributing to anti-Stokes and Stokes signals. The temperature, calculated by using Eq. (7), was found from the anti-Stokes wing, displayed in Fig. S5 (section V in the SI). Interband absorption at 2.4 eV and above depletes anti-Stokes scattering and, therefore, this method must be used with caution as temperature estimates may be biased. The optical heating mechanism is governed by thermalization of charge carries and is also dependent on the slope of the sp-conduction band (Fig. 3f).

Conclusion

In this paper, we have explored the optical heating of spatially dispersive semiconductors and metals driven by inelastic electronic light scattering rather than absorption. The underlying mechanism is indirect optical transitions caused by a change in the electron momentum. This phenomenon, often encountered in SERS/TERS experiments, is perceived as a parasitic background emission.³⁸⁻⁴¹ However, an optical nanoantenna (nanoparticle, quantum dot, defect, etc.) presents a system with strong spatial dispersion, generating broadband inelastic emission that depends on the excitation wavelength and extends over several thousands of cm⁻¹.⁵ This emission, that is specifically the ELS, carries important information on spatial inhomogeneities of nonlocal media, and does not depend on their chemical composition.

Our findings will guide further engineering of white light-emitting diodes and mirrorless lasers at room-temperature,³ silicon solar cells with efficiency beyond the Shockley-Queisser limit^{42,43} and optically transparent conducting electrodes.²⁸ A special attention should be paid to biological systems that are highly heterogeneous. Electronic light scattering opens the route

to optical transparency of biological tissues¹ and optical recognition of peptide and protein conformations.⁴⁴ A promising feature of spatially dispersive media is their optical heating in the transparency window under sub-band pumping. It brings optical heating into sharper focus for thermo-selective treatment of neurodegenerative and oncological diseases.²³

Methods

Gold tip preparation

Gold tips were produced with the home-built voltage controller equipped with a three-electrode electrochemical cell.⁴⁵ This potentiostat allows one to control a current cutoff event as fast as 10 μ s. A piezomanipulator immerses a 100 μ m gold wire (purity: 99.99%, GoodFellow, UK) into a solution of fuming hydrochloric acid (HCl, 37%) and ethanol (C₂H₅OH, 96%) in a volume proportion of 1:1. A unique feature of the electrochemical cell is an inner bottom-free beaker that provides robust and stable, compared with widely used electrochemical cells, etching of a 100 μ m gold wire (purity: 99.99%, GoodFellow, UK) immersed. A ring gold counter-electrode with a diameter of 10 mm, which encompasses the inner beaker, is positioned by a magnitude of 10 mm in depth. Optimal etching regimes for fabricating rough tapered gold tips with the electrochemical cell are reached in the voltage range 1.5–1.7 V to be empirically found for different background electrolytes, materials of electrodes and their mutual arrangement.

Atomic force microscopy

The multimode scanning probe microscope Prima (NT-MDT) was utilized for visualizing a topography of light-structured silicon glasses. AFM cantilever (VIT_P) was made of antimony-doped single crystal silicon (n-type, 0.01-0.025 Ohm-cm). The tip height is 14-16 μ m, the tip curvature radius is 30 nm, the resonant frequency was 300 kHz.

Scanning electron microscopy

The elemental composition, and morphology of the samples were studied by the Auriga Crossbeam Workstation (Carl Zeiss AG, Oberkochen, Germany), equipped with an INCA X-Max silicon drift detector (Oxford Instruments, Abingdon, UK) for energy dispersive X-ray microanalysis. For elemental analysis of Si diodes and wafers, an acceleration voltage of 5keV, an analytical working distance of 4 mm, and an electron probe current of 75 pA were used.

Far-field and near-field Raman spectroscopy and microscopy

Raman spectra and maps were captured with a multi-purpose analytical instrument NTEGRA SPECTRA™ (NT-MDT) in both upright and inverted configuration. The confocal spectrometer was wavelength calibrated with a crystalline silicon (100) wafer by registering the first-order Raman band at 521 cm⁻¹. A sensitivity of the spectrometer was as high as ca. 2500 photon counts per 0.1 s provided that we used a 100× objective (N.A.=0.9), an exit slit (pinhole) of 100 μm and a linearly polarized light with the wavelength of 632.8 nm and the power at the sample of 10 mW. No signal amplification regimes of a Newton EMCCD camera (ANDOR) were used. Low-frequency Raman measurements were performed using a 633 nm Bragg notch filter (OptiGrate) with a spectral blocking window of 10 cm⁻¹.

Disclosures. The authors declare no conflicts of interest.

ACKNOWLEDGEMENT

The authors gratefully thank A.M. Rogov for carrying out SEM measurements, A.I. Fishman and A.B. Shubin for fruitful discussions.

References

1. Ou, Z. et al. Achieving optical transparency in live animals with absorbing molecules. *Science* **385**, eadm6869 (2024).
2. Wang, G. et al. 27.09%-efficiency silicon heterojunction back contact solar cell and going beyond. *Nat. Commun.* **15**, 8931 (2024).
3. Kharintsev, S. S. et al. Extreme electron-photon interaction in disordered perovskites. *Adv. Sci.* 2405709 (2024).
4. Kim, N. et al. Achieving optical refractive index of 10-plus by colloidal self-assembly. *Small* **20**, 2404223 (2024).
5. Kharintsev, S. S. et al. Photon-momentum-enabled electronic Raman scattering in silicon glass. *ACS Nano* **18**, 9557–9565 (2024).
6. Shastri, K. & Monticone, F. Nonlocal flat optics. *Nat. Photonics* **17**, 36–47 (2023).
7. Shim, H., Monticone, F. & Miller, O. D. Fundamental limits to the refractive index of transparent optical materials. *Adv. Mater.* **33**, 2103946 (2021).
8. Khurgin, J. B. Energy and power requirements for alteration of the refractive index. *Laser Photonics Rev.* **18**, 2300836 (2024).
9. Khurgin, J. B. Expanding the photonic palette: exploring high index materials. *ACS Photonics* **9**, 743–751 (2022).

10. Ciraci, C., Pendry, J. B. & Smith, D. R. Hydrodynamic model for plasmonics: a macroscopic approach to a microscopic problem. *ChemPhysChem* **14**, 1109–1116 (2013).
11. Cardona, M. *Light Scattering in Solids I* (Springer-Verlag, Berlin, 1983).
12. Leontovich, M. Generalization of the Kramers-Kronig formulas to media with spatial dispersion. *J. Exptl. Theoret. Phys.* **40**, 907–912 (1961).
13. Di Mei, F. et al. Giant broadband refraction in the visible in a ferroelectric perovskite. *Nat. Photonics* **12**, 734–738 (2018).
14. Kurman, Y. et al. Control of semiconductor emitter frequency by increasing polariton momenta. *Nat. Photonics* **12**, 423–429 (2018).
15. Rivera, N. & Kaminer, I. Light–matter interactions with photonic quasiparticles. *Nat. Rev. Phys.* **2**, 538–561 (2020).
16. Kharintsev, S. S., Battalova, E. I., Mkhitarian, V. & Shalaev, V. M. How near-field photon momentum drives unusual optical phenomena: opinion. *Opt. Mater. Express* **14**, 2017–2022 (2024).
17. Miyata, K., Atallah, T. L. & Zhu, X. Lead halide perovskites: Crystal-liquid duality, phonon glass electron crystals, and large polaron formation. *Sci. Adv.* **3**, e1701469 (2017).
18. Oses, C., Toher, C. & Curtarolo, S. High-entropy ceramics. *Nat. Rev. Mater.* **5**, 295–309 (2020).
19. Canham, L. *Handbook of Porous Silicon* (Springer, New York, 2014).
20. Kharintsev, S. S. et al. Light-controlled multiphase structuring of perovskite crystal enabled by thermoplasmonic metasurface. *ACS Nano* **17**, 9235–9244 (2023).
21. Wilmshurst, J. K. Lattice-type vibrations in associated liquids and the origin of anomalous Rayleigh scattering. *Nature* **192**, 1061–1062 (1961).
22. Bellissent-Funel, M.-C. et al. Water determines the structure and dynamics of proteins. *Chem. Rev.* **116**, 7673–7697 (2016).
23. Eisele, Y. S. et al. Targeting protein aggregation for the treatment of degenerative diseases. *Nat. Rev. Drug Discovery* **14**, 759–780 (2015).
24. Kharintsev, S. S. et al. Photon momentum enabled light absorption in silicon. *ACS Nano* **18**, 26532–26540 (2024).
25. Aouassa, M. et al. Temperature-feedback direct laser reshaping of silicon nanostructures. *Appl. Phys. Lett.* **111**, 243103 (2017).
26. Kharintsev, S. S. et al. Designing two-dimensional temperature profiles using tunable thermoplasmonics. *Nanoscale* **14**, 12117–12128 (2022).
27. Maier, S. *Plasmonics: Fundamentals and Applications* (Springer, New York, 2007).

28. Das, P. et al. Electron confinement–induced plasmonic breakdown in metals. *Sci. Adv.* **10**, eadr2596 (2024).
29. Yamaguchi, M. & Nobusada, K. Indirect interband transition induced by optical near fields with large wave numbers. *Phys. Rev. B* **93**, 195111 (2016).
30. Noda, M., Iida, K., Yamaguchi, M., Yatsui, T. & Nobusada, K. Direct wave-vector excitation in an indirect-band-gap semiconductor of silicon with an optical near-field. *Phys. Rev. Appl.* **11**, 044053 (2019).
31. Magonov, S. N., Elings, V. & Whangbo, M.-H. Phase imaging and stiffness in tapping-mode atomic force microscopy. *Surf. Sci.* **375**, L385–L391 (1997).
32. Cleveland, J. P., Anczykowski, B., Schmid, A. E. & Elings, V. B. Energy dissipation in tapping-mode atomic force microscopy. *Appl. Phys. Lett.* **72**, 2613–2615 (1998).
33. Kamimura, R., Kondo, T., Motobayashi, K. & Ikeda, K. Surface-enhanced electronic Raman scattering at various metal surfaces. *Phys. Status Solidi B* **259**, 2100589 (2022).
34. Inagaki, M. et al. Electronic and vibrational surface-enhanced Raman scattering: from atomically defined Au(111) and (100) to roughened Au. *Chem. Sci.* **11**, 9807–9817 (2020).
35. Penn, D. R. Wave-number-dependent dielectric function of semiconductors. *Phys. Rev.* **128**, 2093–2097 (1962).
36. Sivan, Y. & Chu, S. Nonlinear plasmonics at high temperatures. *Nanophotonics* **6**, 317–328 (2017).
37. Hogan, N. & Sheldon, M. Comparing steady state photothermalization dynamics in copper and gold nanostructures. *J. Chem. Phys.* **152**, 061101 (2020).
38. Amoruso, A. et al. Uncovering low-frequency vibrations in surface-enhanced Raman of organic molecules. *Nat. Commun.* **15**, 6733 (2024).
39. Zhang, R. et al. Chemical mapping of a single molecule by plasmon-enhanced Raman scattering. *Nature* **498**, 82–86 (2013).
40. Lee, J., Crampton, K. T., Tallarida, N. & Apkarian, V. A. Visualizing vibrational normal modes of a single molecule with atomically confined light. *Nature* **568**, 78–82 (2019).
41. Meng, Q. et al. Local heating and Raman thermometry in a single molecule. *Sci. Adv.* **10**, eadl1015 (2024).
42. Ghasemi, M., Jia, B. & Wen, X. Lattice battery solar cells: exceeding Shockley–Queisser limit. *EcoEnergy* **2**, 448–455 (2024).
43. Lee, Y. H. Beyond the Shockley-Queisser limit: exploring new frontiers in solar energy harvest. *Science* **383** <https://www.science.org/doi/10.1126/science.ado4308> (2024).
44. Ma, H. et al. Rapidly determining the 3D structure of proteins by surface-enhanced Raman spectroscopy. *Sci. Adv.* **9**, eadh8362 (2023).

45. Kharintsev, S. S., Noskov, A. I., Hoffmann, G. G. & Loos, J. Near-field optical taper antennas fabricated with a highly replicable ac electrochemical etching method. *Nanotechnology* **22**, 025202 (2011).